

# Crystal Hall effect in Collinear Antiferromagnets

Libor Šmejkal,<sup>1,2,3</sup> Rafael González-Hernández,<sup>4,1</sup> Tomáš Jungwirth,<sup>2,5</sup> and Jairo Sinova<sup>1,2</sup>

<sup>1</sup>*Institut für Physik, Johannes Gutenberg Universität Mainz, D-55099 Mainz, Germany*

<sup>2</sup>*Institute of Physics, Academy of Sciences of the Czech Republic,  
Cukrovarnická 10, 162 00 Praha 6 Czech Republic*

<sup>3</sup>*Faculty of Mathematics and Physics, Charles University in Prague,  
Ke Karlovu 3, 121 16 Prague 2, Czech Republic*

<sup>4</sup>*Grupo de Investigación en Física Aplicada, Departamento de Física, Universidad del Norte, Barranquilla, Colombia*

<sup>5</sup>*School of Physics and Astronomy, University of Nottingham, Nottingham NG7 2RD, United Kingdom*

(Dated: October 19, 2021)

Over a century, Hall effects continue to play a central role in condensed matter research for their intriguing quantum-mechanical, relativistic, and topological nature<sup>1–5</sup>. The anomalous Hall effect requires a set of time and spatial symmetries to be spontaneously broken by the magnetic structure<sup>6–12</sup>. Here we introduce a complementary mechanism in crystals whose magnetic structure alone generates no Hall response and the required breaking of *time-reversal* and other symmetries is caused by the arrangement of *non-magnetic* atoms in the lattice. We present a minimal model of this crystal Hall effect in textbook<sup>13,14</sup> collinear rutile antiferromagnets and, based on our first-principles calculations, we identify crystal Hall conductivity reaching  $\sim 1000$  S/cm in room-temperature antiferromagnetic RuO<sub>2</sub><sup>15,16</sup>. Our theory can also interpret recent Hall measurements in antiferromagnetic CoNb<sub>3</sub>S<sub>6</sub><sup>17</sup>, and we catalogue a broad family of collinear antiferromagnetic candidates for observing the crystal Hall effect. We show that the phenomenon can be controlled by the rearrangement of the crystal structure, lattice chirality, and magnetic order. The robust mechanism of our crystal Hall effect in combination with stable collinear antiferromagnetic order opens a previously unnoticed avenue towards dissipationless quantum transport at ambient conditions.

We start our discussion from pure symmetry perspective to elucidate the basic nature and possibility of observing the crystal Hall effect in a simple collinear antiferromagnet. For this we first recall the equivalence of the magnetic-moment dependent Hall resistivity  $\rho_{ab}(\mathbf{m})$  with a pseudovector parallel to the cross product of the electric field  $\mathbf{E}$  and the Hall current  $\mathbf{j}_H$ ; this is made explicit when writing this dissipationless transport coefficient in the antisymmetrized form<sup>18</sup>,  $\rho_{ab}(\mathbf{m}) = (E_a/j_{H,b} - E_b/j_{H,a})/2$ . Furthermore, the Hall effect requires broken time-reversal ( $\mathcal{T}$ ) symmetry and flips sign under  $\mathcal{T}$ ,  $\rho_{ab}(\mathbf{m}) = -\rho_{ab}(-\mathbf{m})$ . This follows<sup>18</sup> from combining the antisymmetry,  $\rho_{ab}(\mathbf{m}) = -\rho_{ba}(\mathbf{m})$ , with Onsager relations,  $\rho_{ab}(\mathbf{m}) = \rho_{ba}(-\mathbf{m})$ . The Neumann's principle<sup>14</sup> then implies that the anomalous Hall effect is explicitly allowed in ferromagnetic crystals since,

due to the net magnetization pseudovector, its magnetic point group (MPG) has the set of broken time and spatial symmetries required by the Hall resistivity<sup>19</sup>.

The broken symmetry requirement does not imply, however, that the magnitudes of the anomalous Hall effect and net magnetization must be proportional to each other. For example, in Chern insulators, the Berry curvature anomalous Hall conductivity is quantized<sup>4,20</sup>. Another remarkable manifestation is the large contribution to the anomalous Hall effect from a fully compensated non-collinear antiferromagnetic structure<sup>6–12</sup>, as illustrated in Fig. 1a for Mn<sub>3</sub>Pt. Here, apart from breaking the  $\mathcal{T}$ -symmetry, the non-collinear magnetic order lowers all other symmetries required by the Hall resistance pseudovector, leaving, for example, an invariance of the system under spatial rotations about only one axis direction. The net magnetization in the non-collinear structure, illustrated in Fig. 1a, is zero. However, if a net moment was generated by canting the magnetic moments towards the rotational axis, the MPG of the magnetic structure would remain the same. Like in the case of a real net magnetization, the direction of this "ghost" magnetization  $\mathbf{g}$  defines the orthogonal transport plane of the allowed Hall effect in the antiferromagnet.

Our crystal Hall effect can also occur in the absence of a net magnetization. However, the symmetry lowering is not generated by the magnetic structure alone but in combination with the crystal arrangement of non-magnetic atoms. In Fig. 1b we identify a material exhibiting a strong crystal Hall effect, namely the recently discovered room-temperature collinear antiferromagnetic phase in bulk<sup>15</sup> and thin-film<sup>16</sup> of RuO<sub>2</sub>. The material has many practical applications owing to its high electrical conductivity and excellent thermal and chemical stability<sup>15</sup>.

First, we illustrate in Figs. 1e,f the basic principle of  $\mathcal{T}$ -symmetry lowering by non-magnetic atoms in a simplified quasi-1D model of a collinear antiferromagnet. The linear chain shown in Fig. 1e has a  $\mathbf{t}_{\frac{1}{2}}\mathcal{T}$  symmetry, where  $\mathbf{t}_{\frac{1}{2}}$  is the half unit cell translation. In this commonly depicted model, a collinear antiferromagnet belongs to a  $\mathcal{T}$ -symmetric MPG (recall that MPG can be obtained from the magnetic space group by stripping off translations). This excludes any Hall effect induced by spontaneous symmetry breaking. However, as we illustrate

in Fig. 1f, a minimal modification by interlacing the antiferromagnetic moments with zig-zag positions of non-magnetic atoms breaks the  $\mathbf{t}_{\frac{1}{2}}\mathcal{T}$  symmetry and, therefore, breaks the MPG  $\mathcal{T}$ -symmetry.

With this we arrive at the basic distinction on the symmetry level between the anomalous and crystal Hall effects. In the former case, the magnetic structure of a simple ferromagnet like Fe can be represented by a characteristic  $\mathcal{T}$ -symmetry breaking pseudovector whose presence and orientation are independent of the positions of atoms in the crystal. From this symmetry perspective, the crystal structure can be smeared out into a uniform background, in analogy to the Sommerfeld jellium model of a solid. Similarly, the structure of magnetic moments in non-coplanar<sup>5-7</sup> (Fig. 1c) or non-collinear antiferromagnets<sup>5,8-12</sup> (Fig. 1d) can be represented by a characteristic  $\mathcal{T}$ -symmetry breaking pseudovector, in these cases independent of the crystal structure of the non-magnetic atoms. On the other hand, within the picture of a smeared out non-magnetic background, the net effect of collinear antiparallel moments in Fig. 1e cancels out, resulting in an effectively  $\mathcal{T}$ -symmetric system. The  $\mathcal{T}$ -symmetry breaking required by the Hall effect only emerges when we resolve in Fig. 1f the true positions of the non-magnetic atoms in the crystal.

A comparison of Figs. 1f and 1b highlights that, in analogy to the quasi-1D model, oxygen atoms break the MPG  $\mathcal{T}$ -symmetry of the RuO<sub>2</sub> crystal. However, when the Néel vector  $\mathbf{n}$  is along the [001] axis, the RuO<sub>2</sub> crystal is still invariant under rotations about two axes ( $\mathcal{C}_{2x}$ ,  $\mathcal{C}_{2y}$ ). This is not compatible with the presence of a pseudovector which allows for invariance under spatial rotations about only one axis direction (parallel to the pseudovector). The MPG for  $\mathbf{n} \parallel [001]$  has a symmetry which remains too high to allow for a spontaneous Hall effect.

The removal of all symmetries required by the odd pseudovector is achieved when the Néel vector is in the (001) plane. The corresponding MPG,  $m'm'm$ , of our rutile crystal with the Néel vector along the [100] axis can be generated by space-inversion ( $\mathcal{P}$ ), a mirror plane ( $\mathcal{M}_y$ ), and a rotational axis combined with  $\mathcal{T}$  ( $\mathcal{TC}_{2z}$ ). These are marked in Fig. 2a; for the complete list of symmetries see Methods. None of the symmetries breaks when we cant the antiferromagnetic moments towards the [010] direction. This corresponds in the compensated collinear state to the ghost pseudovector  $\mathbf{g} \parallel [010]$  and to a non-zero  $\sigma_{xz}$  component of the crystal Hall conductivity.

In previous paragraphs we verified the possibility for a non-zero crystal Hall effect in a collinear antiferromagnet using exclusively symmetry arguments without even invoking a notion of an electron carrying the charge current. We now proceed to the microscopic analysis, starting from a minimal centro-symmetric 4-band Hamiltonian satisfying the presence of the staggered potential (antiferromagnetic exchange) and the ghost pseudovec-

tor (for more details see Supplementary information):

$$H = t \sum_{ij} c_i^\dagger c_j + J_n \sum_i \mathbf{u}_i \cdot \mathbf{s} c_i^\dagger c_i + \lambda \sum_{ij,k} \mathbf{D}_{ij}^k \cdot \mathbf{s} c_i^\dagger c_j. \quad (1)$$

Here the first term describes electron hopping between nearest neighbor magnetic sites  $i$  and  $j$  on a body centered cubic lattice and the second term describes on-site exchange field with an alternating direction on the neighboring sites,  $\mathbf{u}_i = -\mathbf{u}_j$  ( $\mathbf{s}$  are spin Pauli matrices). These two terms represent a tight-binding model of a collinear antiferromagnet with  $\mathcal{T}$ -symmetry in the MPG.

Extending Haldane's approach<sup>20</sup>, we lower the symmetry of the Hamiltonian (1) by a spin-orbit coupling term in which the vector  $\mathbf{D}_{ij}^k = -\mathbf{D}_{ji}^k$  reflects a local chirality of the electron hopping on a bond  $k$  connecting the nearest neighbor magnetic sites  $i$  and  $j$ . This minimal model, shown in Fig. 2b, is general for describing the crystal Hall effect in a collinear antiferromagnet. However, we can also give the vector  $\mathbf{D}_{ij}^k$  a specific material interpretation by referring to our RuO<sub>2</sub> crystal. Here,  $\mathbf{D}_{ij}^k = \mathbf{d}_i \times \mathbf{d}_j$ , where  $\mathbf{d}_i$  and  $\mathbf{d}_j$  are unit vectors connecting two nearest-neighbor Ru atoms with the common interlaced oxygen atom (cf. Fig. 2a and 2b). The corresponding Hamiltonian in the crystal-momentum space reads,

$$H_{\mathbf{k}} = -4t\tau_x \cos \frac{k_x}{2} \cos \frac{k_y}{2} \cos \frac{k_z}{2} + \tau_z J_n \mathbf{s} \cdot \mathbf{n} + 4i\lambda\tau_x \sin \frac{k_z}{2} \left[ s_{xy}^{(-)} \sin \frac{k_x+k_y}{2} + s_{xy}^{(+)} \sin \frac{k_x-k_y}{2} \right], \quad (2)$$

where  $\tau$  are site Pauli matrices and  $s_{xy}^{(\pm)} = s_x \pm s_y$ .

The combination of exchange and spin-orbit coupling (second and third term in Eq. (2)) breaks the MPG  $\mathcal{T}$ -symmetry which lifts Kramer's band degeneracy for all directions of  $\mathbf{n}$ <sup>11,21</sup>. However, the crystal Hall effect is allowed only when  $\mathbf{n}$  has a projection to the (001) plane. We show this on the intrinsic (independent of disorder-scattering) Hall conductivity which is obtained by integrating the Berry curvature,  $\Omega(\mathbf{k}) = -\text{Im}\langle \partial_{\mathbf{k}} u(\mathbf{k}) | \times | \partial_{\mathbf{k}} u(\mathbf{k}) \rangle$ , in the crystal momentum space (see Methods). For  $\mathbf{n} \parallel [100]$ , the application of symmetry operations  $\mathcal{M}_y$ ,  $\mathcal{P}$  and  $\mathcal{TC}_{2z}$  implies that  $\int dk_x \Omega_x(\mathbf{k}) = 0$ , while symmetry operations  $\mathcal{M}_y$ , and  $\mathcal{TC}_{2z}\mathcal{M}_y$  yield  $\int dk_z \Omega_z(\mathbf{k}) = 0$ . The non-vanishing integral is for the  $\Omega_y(\mathbf{k})$ -component. We illustrate this in Fig. 2c showing that  $\int dk_x \Omega_y(\mathbf{k})$  is even in  $k_y$ .

The magnitude of the crystal Hall effect depends on the band structure, which reflects the magnetic space group (MSG) symmetries. For  $\mathbf{n} \parallel [100]$ , our system is invariant under non-symmorphic symmetry operations (e.g. a mirror plane coupled to a half-unit cell translation  $\mathcal{M}_y \mathbf{t}_{\frac{1}{2}}$ ). On the other hand, for  $\mathbf{n} \parallel [110]$ , the system has symmorphic symmetries (e.g.  $\mathcal{M}_{x\bar{y}}$ ). This results, for  $\mathbf{n} \parallel [100]$ , in an antiferromagnetic generalization of the nodal-chain band structure<sup>22</sup> (see Fig. 2d), while, for  $\mathbf{n} \parallel [1\bar{1}0]$ , the band structure has two non-connected nodal lines (see Fig. 2e). The corresponding spin-orbit entangled bands around the nodal-lines generate a Berry curvature effective field in crystal momentum space akin

to an ordinary magnetic field generated by real space loop currents. The reconfiguration of the nodal-lines between  $\mathbf{n} \parallel [100]$  and  $[1\bar{1}0]$  results in a dramatic change in Berry curvature maps, as shown in Figs. 2d,e.

We now verify the results of our model analyses by first-principles calculations in the real crystal of  $\text{RuO}_2$  (for more details see Methods and Supplementary information). Note that among the rutile oxides, a metallic phase is rare which makes the recently discovered<sup>15,16</sup> itinerant antiferromagnetism in  $\text{RuO}_2$  exceptional within this family of simple collinear antiferromagnets. Our density functional theory (DFT) calculations show that for a medium strength Hubbard parameter ( $U = 2$  eV), antiferromagnetism and metallic density of states (DOS) coexist, consistent with previous reports<sup>15,16</sup>.

The first-principles Berry curvature shown in Fig. 3a exhibits analogous symmetry as the model results (cf. Fig. 2c and Supplementary information). In Fig. 3b, we plot the band structure along the  $\Gamma XSYTZ$  line for  $\mathbf{n} \parallel [100]$ , and  $[110]$ . Again in analogy to the model results, the hybridization of linear band crossings and the gapping of nodal-line features<sup>23</sup> strongly depends on the Néel vector orientation<sup>21</sup> and reflects the change from a non-symmorphic MSG for  $\mathbf{n} \parallel [100]$  ( $Pnn'm'$ ) to a symmorphic MSG for  $\mathbf{n} \parallel [110]$  ( $Cnn'm'$ ).

In Fig. 3c we plot the intrinsic crystal Hall conductivity calculated from first-principles by employing Wannier functions (see Methods). Numerical data are plotted as a function of the Fermi level position which simulates, e.g., alloying. We observe peak values of  $\sim 1000$  S/cm, corresponding to the record magnitudes reported for the anomalous Hall effect in ferromagnets or non-collinear antiferromagnets<sup>2,9</sup>.

When turning the sizable spin-orbit coupling off in our DFT calculation, we observe a perfect antiferromagnetic compensation in the Ru-projected DOS, as shown in Fig. 3d. With the large atomic spin-orbit coupling turned on, only minute corrections to the DOS occur. They result in a small net magnetic moment,  $\mathbf{m} = \mathbf{m}_A + \mathbf{m}_B$ , of a magnitude  $\sim 0.05 \mu_B$  due to Dzyaloshinskii-Moriya interaction (DMI)<sup>24</sup>. Here  $\mathbf{m}_{A/B}$  are magnetizations of the antiferromagnetic  $A$  and  $B$  sublattices. In comparison, the Néel vector  $\mathbf{n} = (\mathbf{m}_A - \mathbf{m}_B)/2$  has a magnitude  $\sim 1.17 \mu_B$ . To gain further insight, we calculate the dependence of the crystal Hall effect for  $\mathbf{n} \parallel [100]$  on the canting angle between magnetizations of sublattices  $A$  and  $B$  (see Fig. 3e). For artificially constrained perfectly antiparallel moments,  $\mathbf{g} \parallel [010]$  and we obtain  $\sigma_{xz} = 36.4 \text{ Scm}^{-1}$ . For a canting angle  $\approx 1^\circ$  obtained from the DFT calculation,  $\mathbf{m} \parallel [010]$  and  $\sigma_{xz} = 35.7 \text{ Scm}^{-1}$ . The small net magnetic moment has a negligible effect on  $\sigma_{xz}$ . This is in striking contrast to the recently studied antiferromagnets  $\text{GdPtBi}$ <sup>25</sup> and  $\text{EuTiO}_3$ <sup>26</sup> which order in a  $\mathcal{T}$ -invariant MPG and whose observed anomalous Hall effect is entirely due to the canting induced by an applied external magnetic field.

To measure the crystal Hall effect in  $\text{RuO}_2$  with the Néel vector in the (001)-plane, an in-plane magnetic field

can be applied to select via canting one of the two domains with opposite in-plane Néel vectors and corresponding opposite signs of the Hall effect, as explained in Fig. 3f. However, since stoichiometric  $\text{RuO}_2$  can have an out-of-plane easy-axis<sup>15</sup>, an additional spin-flop field has to be applied along the [001]-axis to force the Néel vector into the (001)-plane. Alternatively, our DFT calculations show (see Supplementary information) that by a few per cent alloying, e.g.  $\text{Ru}_{1+x}\text{O}_{2-x}$  or  $\text{Ru}_{1-x}\text{Ir}_x\text{O}_2$ , the easy axis can switch from the [001] direction to the (001) plane. This also demonstrates the possibility to turn the crystal Hall effect on and off by reorienting the Néel vector. In contrast, the anomalous Hall effect in ferromagnets is allowed by symmetry for any direction of the magnetization.

We next discuss the possibility to control the crystal Hall effect by the arrangement of nonmagnetic atoms. Our first principle calculations (for detailed angular dependencies see Supplementary information) explicitly highlight that the crystal Hall effect flips sign when reversing the Néel vector in  $\text{RuO}_2$ , consistent with Onsager relations. Remarkably, the sign of the crystal Hall effect changes also when keeping the Ru moments fixed and, instead, rearranging the crystal positions of oxygen atoms in a way that reverses the local real-space chirality of their positions, as shown in the Fig. 4a,b. We point out that the two crystal structures transform one to the other via a roto-reversal symmetry operation<sup>27</sup> ( $1^\Phi$ ). This operation is not present in the conventional MPG nomenclature<sup>27</sup> and is composed of rotating each of the two oxygen octahedra in the opposite sense by  $90^\circ$  (see Supplementary information). The symmetry ensures the same magnitude of  $\sigma_{xz}$  when the local chirality of the oxygen positions (the sign of  $\mathbf{D}_{ij}^k$  in the model) is reversed. From this, we can draw a comparison to the anomalous Hall effect in ferromagnets, where the sign reversal of the Hall conductivity is governed by the reversal of  $\mathbf{m}$ . The sign of the crystal Hall effect in  $\text{RuO}_2$  is, instead, determined by the sign of  $\mathbf{n} \cdot \mathbf{D}_{ij}^k$ , again underlining the crystal mechanism of the symmetry breaking in this collinear antiferromagnet.

We now illustrate that our crystal Hall effect mechanism can shed light also on the already existing experimental data in more complex antiferromagnets. This applies, e.g., to the measured spontaneous Hall signal in a doped canted antiferromagnet  $\text{CaMnO}_3$  (MPG  $2'/m'$ )<sup>28</sup>. Apart from the anomalous Hall contribution due to the net magnetic moment, our symmetry analysis shows that the crystal Hall effect associated with the Néel vector rather than the canting moment (c.f. Fig. 3e) is allowed in this material. Another example is the spontaneous Hall effect recently detected in  $\text{CoNb}_3\text{S}_6$  antiferromagnet<sup>17</sup> (see Fig. 4c) which could not be reconciled with a collinear antiferromagnetic order inferred from neutron scattering<sup>29</sup>. According to our analysis, however,  $\text{CoNb}_3\text{S}_6$  can have the required set of broken MPG symmetries even in a collinear antiferromagnetic phase due to the arrangement of the S atoms. Our first-

principles calculations shown in Fig. 4d give a magnitude of the crystal Hall effect in hole-doped  $\text{CoNb}_3\text{S}_6$  which is consistent with the experimental value ( $27 \text{ S/cm}^{17}$ ). Our calculations shown in Fig. 4d also confirm the expected sign change of the crystal Hall effect when we swap the *global* crystal chirality from the left-handed to the right-handed (see Fig. 4c).

We point out that as many as  $\sim 10\%$  of the total of  $\sim 600$  magnetic structures reported in the Bilbao Magn-Data database<sup>30</sup> are collinear antiferromagnets in which the crystal Hall effect is allowed by symmetry. All 31 MPGs that can host the electrical crystal Hall effect, as well as its optical and thermal counterparts<sup>5</sup>, and real material examples are listed in the Supplementary information. The ghost vector in 25 out of these MPGs is either perpendicular to the mirror plane (see Fig. 1b), or parallel to the  $n$ -fold rotational axis (see Fig. 4c).

Finally, we recall that the research of topological Hall currents holds a promise of dissipationless nanoelectronics<sup>2,4</sup>. However, the previously identified mechanisms have been impractical, requiring either excessive magnetic fields in case of the quantum Hall effect or relying on a fragile low-temperature magnetic order in the quantum anomalous Hall effect<sup>4</sup>. Our crystal Hall effect points to a paradigm change in this research area as it introduces a robust mechanism of the required spontaneous symmetry breaking, compatible with a stable collinear antiferromagnetic order.

## METHODS

Our full tight binding model in Eq. (2), including the spin-orbit coupling, can be solved analytically, and we obtain four-energy-bands:

$$\pm \sqrt{T_{\mathbf{k}}^2 + J_n^2 + \Lambda_{\mathbf{k}}^2} \pm \sqrt{4(J_z^2 + T_{\mathbf{k}}^2)\Lambda_{\mathbf{k}}^2 + 4(J_y\Lambda_{1,\mathbf{k}} - J_x\Lambda_{2,\mathbf{k}})},$$

where

$$\begin{aligned} J_n^2 &= J_x^2 + J_y^2 + J_z^2, \\ T_{\mathbf{k}} &= 4t \cos k_x/2 \cos k_y/2 \cos k_z/2, \\ \Lambda_{1,\mathbf{k}} &= 8\lambda \sin k_z/2 \cos k_x/2 \sin k_y/2, \\ \Lambda_{2,\mathbf{k}} &= 8\lambda \sin k_z/2 \sin k_x/2 \cos k_y/2, \\ \Lambda_{\mathbf{k}} &= \Lambda_{1,\mathbf{k}} + i\Lambda_{2,\mathbf{k}}. \end{aligned}$$

The MSG of rutile antiferromagnets for the Néel vector along the [100] and [110] axis, respectively, are:

$$Pnn'm' : \mathcal{P}, \mathcal{G}_y, \mathcal{S}_{2y}, \mathcal{TC}_{2z}, \mathcal{TM}_z, \mathcal{TG}_x, \mathcal{TS}_{2x},$$

$$Cmm'm' : \mathcal{P}, \mathcal{M}_{xy}, \mathcal{C}_{2xy}, \mathcal{TC}_{2z}, \mathcal{TM}_z, \mathcal{TM}_{\bar{xy}}, \mathcal{TC}_{2\bar{xy}},$$

where the non-symmorphic symmetries are the unitary glide plane  $\mathcal{G}_y = \mathcal{M}_y \mathbf{t}_{\frac{1}{2}}$ , screw rotation  $\mathcal{S}_{2y} = \mathcal{C}_{2y} \mathbf{t}_{\frac{1}{2}}$ , and anti-unitary  $\mathcal{TG}_x = \mathcal{TM}_x \mathbf{t}_{\frac{1}{2}}$ , and  $\mathcal{TS}_{2x} = \mathcal{TC}_{2x} \mathbf{t}_{\frac{1}{2}}$  and in the case of  $Cmm'm'$  there are also operations coupled by  $\mathbf{t} = (1/2, 1/2, 0)$ .

The MSG of  $\text{CoNb}_3\text{S}_6$  for the Néel vector along the [100] is  $C2'2'2_1$  and includes symmetry operations  $\mathcal{TC}_{2x}$ ,  $\mathcal{TS}_{2y}$ , and  $\mathcal{S}_{2z}$ , where  $\mathbf{t} = (0, 0, 1/2)$  and all the symmetries coupled by  $\mathbf{t} = (1/2, 1/2, 0)$ . The magnetic Laue group (MPG stripped off inversions) is the same,  $2'2'2$ , for both  $\text{RuO}_2$ , and  $\text{CoNb}_3\text{S}_6$  crystal, and thus also the shape of the conductivity tensor.

The time reversal operation acts on the Berry curvature as  $\mathcal{T}\Omega(\mathbf{k}) = -\Omega(-\mathbf{k})$ , and the following symmetries operate as:

$$\begin{aligned} \mathcal{P}\Omega(\mathbf{k}) &= \Omega(-\mathbf{k}), \\ \mathcal{M}_y\Omega(\mathbf{k}) &= (-\Omega_x, \Omega_y, -\Omega_z)(k_x, -k_y, k_z), \\ \mathcal{C}_{2y}\Omega(\mathbf{k}) &= (-\Omega_x, \Omega_y, -\Omega_z)(-k_x, k_y, -k_z), \\ \mathcal{TC}_{2z}\Omega(\mathbf{k}) &= (\Omega_x, \Omega_y, -\Omega_z)(k_x, k_y, -k_z), \\ \mathcal{TM}_z\Omega(\mathbf{k}) &= (\Omega_x, \Omega_y, -\Omega_z)(-k_x, -k_y, k_z), \\ \mathcal{TM}_x\Omega(\mathbf{k}) &= (-\Omega_x, \Omega_y, \Omega_z)(k_x, -k_y, -k_z), \\ \mathcal{TC}_{2x}\Omega(\mathbf{k}) &= (-\Omega_x, \Omega_y, \Omega_z)(-k_x, k_y, k_z). \end{aligned}$$

We calculated the Hall conductivity in our model and in DFT as,

$$\sigma_{xz} = -\frac{e^2}{\hbar} \int \frac{d\mathbf{k}}{(2\pi)^3} \sum_n f(\mathbf{k}) \Omega_y(n, \mathbf{k}), \quad (3)$$

where the Berry curvature,  $\Omega_y(n, \mathbf{k})$ , is defined as in the main text for each individual band with the quantum number  $n$  and corresponding Bloch functions  $u_n(\mathbf{k})$ , and  $f(\mathbf{k})$  is the Fermi-Dirac distribution<sup>31</sup>.

We have calculated the electronic structure of  $\text{RuO}_2$  in the full potential DFT code ELK<sup>32</sup> and pseudopotential DFT code VASP<sup>33</sup>, within PBE+U+SOC (spherically invariant version of DFT+U)<sup>34</sup> on a  $12 \times 12 \times 16$   $k$ -point grid and we use energy cut-off 500 eV. In the case of  $\text{RuO}_2$  crystal, we performed our magnetocrystalline anisotropy calculations on a  $16 \times 16 \times 24$   $k$ -point grid. For the transport calculations, we used only VASP results. We obtained Wannier functions on a  $12 \times 12 \times 16$  grid using the Wannier90 code<sup>35</sup> and we calculated the Hall conductivity by employing Eq. (3) evaluated on the Monkhorst-Pack grid with a  $321^3$  crystal momentum integration mesh in Wannier tools<sup>36</sup>. In the case of  $\text{CoNb}_3\text{S}_6$ , we evaluate Wannier functions on a  $12 \times 12 \times 6$  grid, and we use  $241^2 \times 201$  crystal momentum points for the Hall conductivity calculation. We tested our first principles calculation methodology on the experimentally and theoretically investigated anomalous Hall conductivity in ferromagnets and non-collinear antiferromagnets and we obtained an agreement with the previous reports (e.g., 234 S/cm in  $\text{IrMn}_3$ , cf. Ref. 11).

## ACKNOWLEDGMENTS

We acknowledge discussions with M. Kläui, M. Jourdan, G. Jakob, J. Železný, Y. Mokrousov, and S. Stemmer. We acknowledge the use of the supercomputer

Mogon at JGU (hpc.uni-mainz.de), the computing and storage facilities owned by parties and projects contributing to the National Grid Infrastructure MetaCentrum provided under the programme "Projects of Projects of Large Research, Development, and Innovations In-

frastructures" (CESNET LM2015042) and support from the Alexander von Humboldt Foundation, the Transregional Collaborative Research Center (SFB/TRR) 173 SPIN+X, EU FET Open RIA Grant no. 766566, the Grant Agency of the Charles University Grant no. 280815 and of the Czech Science Foundation Grant no. 14-37427.

- <sup>1</sup> Hall, E. H. On a New Action of the Magnet on Electric Currents. *Am. J. Math.* **2**, 287 (1879). URL <https://www.jstor.org/stable/2369245?origin=crossref>.
- <sup>2</sup> Nagaosa, N., Sinova, J., Onoda, S., MacDonald, A. H. & Ong, N. P. Anomalous Hall effect. *Rev. Mod. Phys.* **82**, 1539–1592 (2010). URL <http://link.aps.org/doi/10.1103/RevModPhys.82.1539>.
- <sup>3</sup> von Klitzing, K. The quantized hall effect. *Rev. Mod. Phys.* **58**, 519–531 (1986). URL <https://link.aps.org/doi/10.1103/RevModPhys.58.519>.
- <sup>4</sup> Wang, J. & Zhang, S.-C. Topological states of condensed matter. *Nature Materials* **16**, 1062–1067 (2017). URL <http://www.nature.com/doi/10.1038/nmat5012>.
- <sup>5</sup> Šmejkal, L., Mokrousov, Y., Yan, B. & MacDonald, A. H. Topological antiferromagnetic spintronics. *Nat. Phys.* **14**, 242–251 (2018). URL <http://dx.doi.org/10.1038/s41567-018-0064-5>. 1706.00670.
- <sup>6</sup> MacHida, Y., Nakatsuji, S., Onoda, S., Tayama, T. & Sakakibara, T. Time-reversal symmetry breaking and spontaneous Hall effect without magnetic dipole order. *Nature* **463**, 210–213 (2010).
- <sup>7</sup> Sürgers, C., Fischer, G., Winkel, P. & Löhneysen, H. V. Large topological Hall effect in the non-collinear phase of an antiferromagnet. *Nat. Commun.* **5**, 3400 (2014).
- <sup>8</sup> Nakatsuji, S., Kiyohara, N. & Higo, T. Large anomalous Hall effect in a non-collinear antiferromagnet at room temperature. *Nature* **527**, 212–215 (2015). URL <http://www.nature.com/doi/10.1038/nature15723>.
- <sup>9</sup> Nayak, A. K. *et al.* Large anomalous Hall effect driven by a nonvanishing Berry curvature in the noncollinear antiferromagnet Mn<sub>3</sub>Ge. *Sci. Adv.* **2**, e1501870–e1501870 (2016). URL <http://advances.sciencemag.org/cgi/doi/10.1126/sciadv.1501870>. 1511.03128.
- <sup>10</sup> Liu, Z. Q. *et al.* Electrical switching of the topological anomalous Hall effect in a non-collinear antiferromagnet above room temperature. *Nat. Electron.* **1**, 172–177 (2018). URL <http://www.nature.com/articles/s41928-018-0040-1>.
- <sup>11</sup> Chen, H., Niu, Q. & MacDonald, A. H. Anomalous Hall Effect Arising from Noncollinear Antiferromagnetism. *Phys. Rev. Lett.* **112**, 017205 (2014). URL <http://link.aps.org/doi/10.1103/PhysRevLett.112.017205><https://link.aps.org/doi/10.1103/PhysRevLett.112.017205>.
- <sup>12</sup> Kübler, J. & Felser, C. Non-collinear antiferromagnets and the anomalous Hall effect. *Europhys. Lett.* **108**, 67001 (2014). URL <http://stacks.iop.org/0295-5075/108/i=6/a=67001?key=crossref.7fc151e16858620dbeae03d11c5917a6.1410.5985>.
- <sup>13</sup> Tinkham, M. *Group Theory and Quantum Mechanics*. Dover Books on Chemistry and Earth Sciences (Dover Publications, 2003).
- <sup>14</sup> Bradley, C. & Cracknell, A. *The mathematical theory of symmetry in solids: representation theory for point groups and space groups* (Clarendon Press, 1972).
- <sup>15</sup> Berlijn, T. *et al.* Itinerant Antiferromagnetism in RuO<sub>2</sub>. *Phys. Rev. Lett.* **118**, 077201 (2017). 1612.09589.
- <sup>16</sup> Zhu, Z. H. *et al.* Anomalous Antiferromagnetism in Metallic RuO<sub>2</sub> Determined by Resonant X-ray Scattering. *ArXiv e-prints* (2018). URL <http://arxiv.org/abs/1806.02036>. 1806.02036.
- <sup>17</sup> Ghimire, N. J. *et al.* Large anomalous Hall effect in the chiral-lattice antiferromagnet CoNb<sub>3</sub>S<sub>6</sub>. *Nat. Commun.* **9**, 3280 (2018). URL <http://www.nature.com/articles/s41467-018-05756-7>.
- <sup>18</sup> Shtrikman, S. & Thomas, H. Remarks on linear magnetoresistance and magneto-heat-conductivity. *Solid State Commun.* **3**, 147–150 (1965). URL <http://linkinghub.elsevier.com/retrieve/pii/003810986590178X>.
- <sup>19</sup> Grimmer, H. General relations for transport properties in magnetically ordered crystals. *Acta Crystallographica Section A* **49**, 763–771 (1993).
- <sup>20</sup> Haldane, F. D. M. Model for a Quantum Hall Effect without Landau Levels: Condensed-Matter Realization of the {‘Parity Anomaly’}. *Phys. Rev. Lett.* **61**, 2015 (1988). URL <http://link.aps.org/doi/10.1103/PhysRevLett.61.2015>.
- <sup>21</sup> Šmejkal, L., Železný, J., Sinova, J. & Jungwirth, T. Electric Control of Dirac Quasiparticles by Spin-Orbit Torque in an Antiferromagnet. *Phys. Rev. Lett.* **118**, 106402 (2017). 1610.08107.
- <sup>22</sup> Bzdušek, T., Wu, Q. S., Rüegg, A., Sigrist, M. & Soluyanov, A. A. Nodal-chain metals. *Nature* **538**, 75–78 (2016). URL <http://dx.doi.org/10.1038/nature19099>. 1604.03112.
- <sup>23</sup> Kim, K. *et al.* Large anomalous Hall current induced by topological nodal lines in a ferromagnetic van der Waals semimetal. *Nat. Mater.* **17**, 794 – 799 (2018).
- <sup>24</sup> IE Dzyaloshinskii. The Magnetic Structure of Fluorides of the Transition Metals. *Sov. Phys. JETP* **6**, 1120–1122 (1958).
- <sup>25</sup> Suzuki, T. *et al.* Large anomalous Hall effect in a half-Heusler antiferromagnet. *Nat. Phys.* **12**, 1119 (2016). URL <http://www.nature.com/doi/10.1038/nphys3831>.
- <sup>26</sup> Takahashi, K. S. *et al.* Anomalous Hall effect derived from multiple Weyl nodes in high-mobility EuTiO<sub>3</sub> films. *Sci. Adv.* **4**, eaar7880 (2018). URL <http://advances.sciencemag.org/lookup/doi/10.1126/sciadv.aar7880>.
- <sup>27</sup> Gopalan, V. & Litvin, D. B. Rotation-reversal symmetries in crystals and handed structures. *Nat. Mater.* **10**, 376–381 (2011). 1007.3544.
- <sup>28</sup> Vistoli, L. *et al.* Giant topological Hall effect in correlated oxide thin films. *Nat. Phys.* 6772 (2018). URL <http://www.nature.com/articles/s41567-018-0307-5>.
- <sup>29</sup> Parkin, S. S. P., Marseglia, E. A. & Brown, P. J. Magnetic structure of Co 1/3 NbS<sub>2</sub> and Co 1/3 TaS<sub>2</sub>. *J.*

- Phys. C Solid State Phys.* **16**, 2765–2778 (1983). URL <http://stacks.iop.org/0022-3719/16/i=14/a=016?key=crossref.c4c861bd059d03203badce9b893b4617>.
- <sup>30</sup> Gallego, S. V. *et al.* MAGNDATA : towards a database of magnetic structures. II. The incommensurate case. *J. Appl. Crystallogr.* **49**, 1941–1956 (2016). URL <http://scripts.iucr.org/cgi-bin/paper?S1600576716015491>.
- <sup>31</sup> Coh, S., Vanderbilt, D. & *et al.* Pythtb URL [http://physics.rutgers.edu/pythtb/\\_downloads/pythtb-formalism.pdf](http://physics.rutgers.edu/pythtb/_downloads/pythtb-formalism.pdf).
- <sup>32</sup> <http://elk.sourceforge.net>.
- <sup>33</sup> Kresse, G. & Hafner, J. Ab initio molecular dynamics for liquid metals. *Phys. Rev. B* **47**, 558–561 (1993). 0927-0256(96)00008.  
Kresse, G. & Hafner, J. Norm-conserving and ultrasoft pseudopotentials for first-row and transition elements. *J. Phys. Condens. Matter* **6**, 8245–8257 (1994).  
Kresse, G. & Furthmüller, J. Efficiency of ab-initio total energy calculations for metals and semiconductors using a plane-wave basis set. *Comput. Mater. Sci.* **6**, 15–50 (1996). 0927-0256(96)00008.  
Kresse, G. & Furthmüller, J. Efficient iterative schemes for ab initio total-energy calculations using a plane-wave basis set. *Phys. Rev. B - Condens. Matter Mater. Phys.* **54**, 11169–11186 (1996). 0927-0256(96)00008.
- <sup>34</sup> Kresse, G. & Hafner, J. Ab initio molecular-dynamics simulation of the liquid-metalamorphous-semiconductor transition in germanium. *Phys. Rev. B* **49**, 14251–14269 (1994). URL <http://link.aps.org/doi/10.1103/PhysRevB.49.14251>. 0927-0256(96)00008.  
Kresse, G.; Joubert, D. From ultrasoft pseudopotentials to the projector augmented-wave method. *Phys. Rev. B - Condens. Matter Mater. Phys.* **59**, 1758–1775 (1999). 0927-0256(96)00008.
- <sup>35</sup> Mostofi, A. A. *et al.* An updated version of wannier90: A tool for obtaining maximally-localised Wannier functions. *Comput. Phys. Commun.* **185**, 2309–2310 (2014). URL <http://dx.doi.org/10.1016/j.cpc.2014.05.003>. 0708.0650.
- <sup>36</sup> Wu, Q., Zhang, S., Song, H.-F., Troyer, M. & Soluyanov, A. A. Wanniertools : An open-source software package for novel topological materials. *Computer Physics Communications* **224**, 405 – 416 (2018). URL <http://www.sciencedirect.com/science/article/pii/S0010465517303442>.

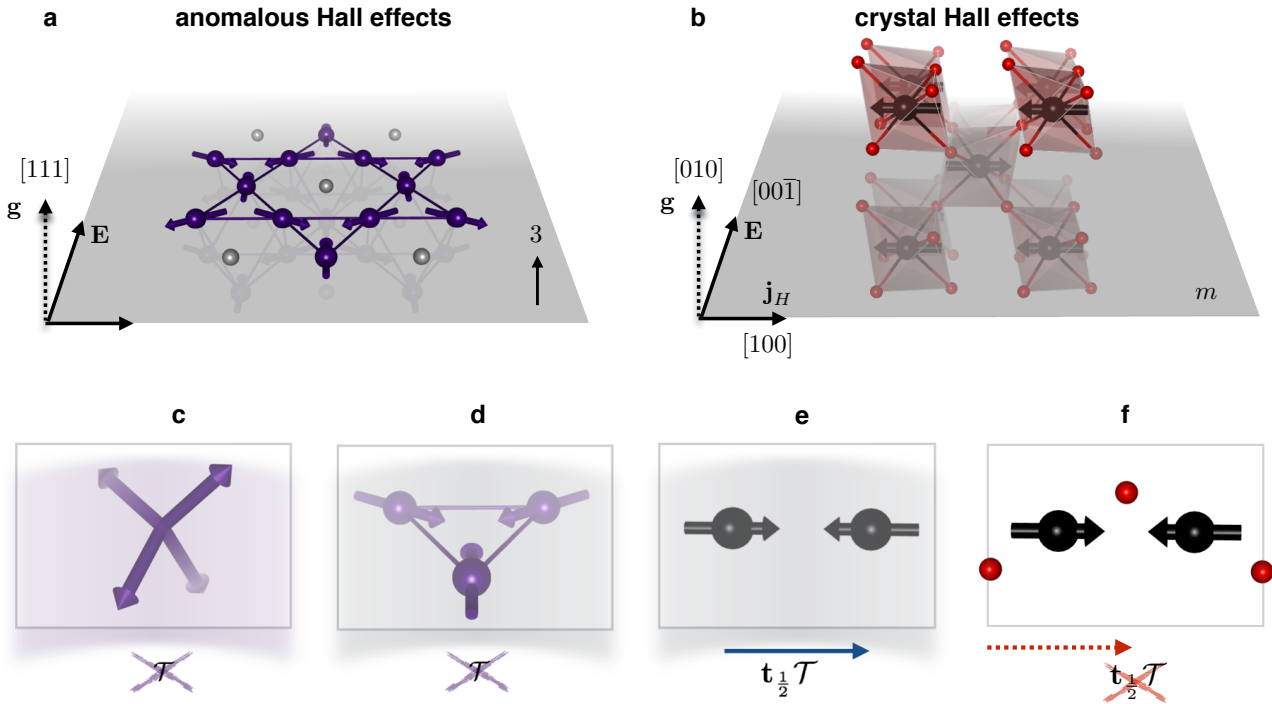


FIG. 1. **Anomalous and crystal Hall effects.** **a**, Anomalous Hall effect due to a ghost vector ( $\mathbf{g}$ ) generated by the non-collinear antiferromagnetic order (purple arrows) in  $\text{Mn}_3\text{Pt}$  (Mn: purple spheres, Pt: grey spheres). **b**, Crystal Hall effect due to the ghost vector generated by the crystal structure of  $\text{RuO}_2$  (Ru: black spheres, O: red spheres) with a collinear antiferromagnetic order (black arrows). **c**, Non-coplanar antiferromagnetic moments, and **d**, triangular magnetic moment arrangement of panel **a** effectively treated as a magnetic medium generates a characteristic  $\mathcal{T}$ -symmetry breaking pseudovector superimposed on a Sommerfeld "jellium" model of the solid (blurred background). **e**, The time-reversal coupled with half-unit cell translation,  $\mathcal{T}\mathbf{t}_{\frac{1}{2}}$ , is symmetry in a simple 1D model of a collinear antiferromagnet. Within the "jellium" model of a smeared out nucleus background (blurred grey), the mean effect of collinear antiparallel moments cancels out, resulting in an effectively  $\mathcal{T}$ -symmetric medium. **f**, Crystal breaking of the  $\mathcal{T}\mathbf{t}_{\frac{1}{2}}$  symmetry by non-magnetic atoms (red spheres) in a quasi 1D model of a collinear antiferromagnet. The symmetry breaking only emerges when we abandon the "jellium" model and resolve the true atomic positions (highlighted in red) in the solid.

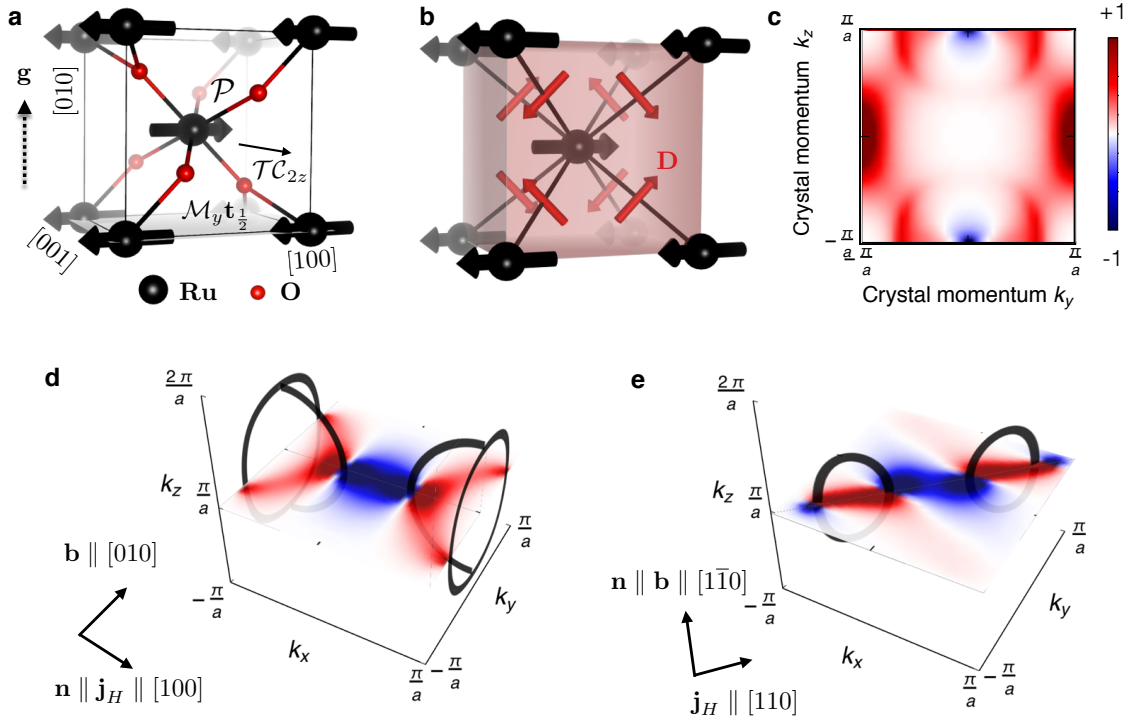


FIG. 2. **Minimal model calculations of the crystal Hall effect.** **a**, The unit cell of antiferromagnetic RuO<sub>2</sub> with the Néel vector along the [100]-axis and marked crystal symmetries. **b**, A minimal model of a collinear antiferromagnetic order (black arrows) and spin-orbit fields (red arrows) corresponding in RuO<sub>2</sub> to the local chirality of the electron hopping on a bond connecting the nearest neighbor sites of magnetic sublattices. **c**, Model calculations of  $\int dk_x \Omega_y(\mathbf{k})$  (in a.u.) for the Néel vector along the [100]-axis, revealing the crystal Hall conductivity  $\sigma_{xz} \neq 0$ . **d**, Berry curvature component  $\Omega_y$  at the  $k_z = \pi$  plane (color plot) and nodal lines in the electronic bands (black lines) for the Néel vector along the [100]-axis. **e**, Same as **d** for the Néel vector along the  $[1\bar{1}0]$ -axis. The model parameters are:  $\lambda = 0.4t$   $J_n = 1.7$ .

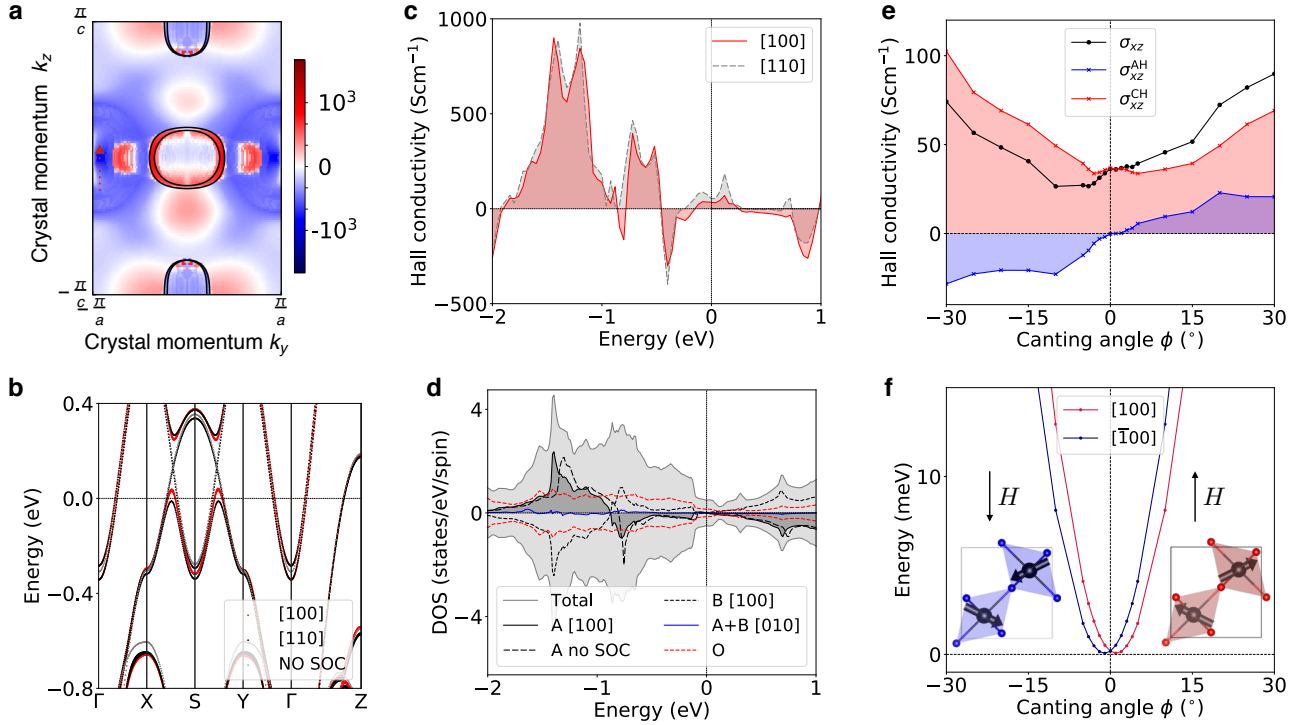


FIG. 3. **First principles calculations of the electronic structure and crystal Hall effect in RuO<sub>2</sub>.** **a**, Calculations of  $\int dk_x b_y(\mathbf{k})$ . **b**, Electronic bands plotted for  $\mathbf{n} \parallel [100]$  and  $[110]$ . **c**, Energy dependence of the calculated crystal Hall conductivity for  $\mathbf{n} \parallel [100]$  (red solid line) and  $\mathbf{n} \parallel [110]$  (gray dashed line). **d**, Ru sublattice *A* (solid) and *B* (dashed) projected DOSs for the Néel vector along the  $[100]$  axis. Black dashed line is for calculation without spin-orbit coupling. Black solid and dotted lines show calculations with spin-orbit coupling of the DOS component for moments projected along the  $[100]$  axis. Blue line shows the sum of sublattice DOSs for the moment projection along the  $[010]$  axis which corresponds to the small canting of the antiparallel moments due to DMI. **e**, The dependence on the canting angle of the Hall conductivity and its separation into the anomalous (ferromagnetic) and crystal (antiferromagnetic) parts. **f**, Two magnetic domains with opposite Néel vector induced by opposite field  $H$  and the corresponding energy costs for canting.  $H \parallel [010]$  corresponds to canting angles  $\phi > 0$  and prefers  $\mathbf{n} \parallel [100]$  (red) over  $\mathbf{n} \parallel [\bar{1}00]$  (blue).

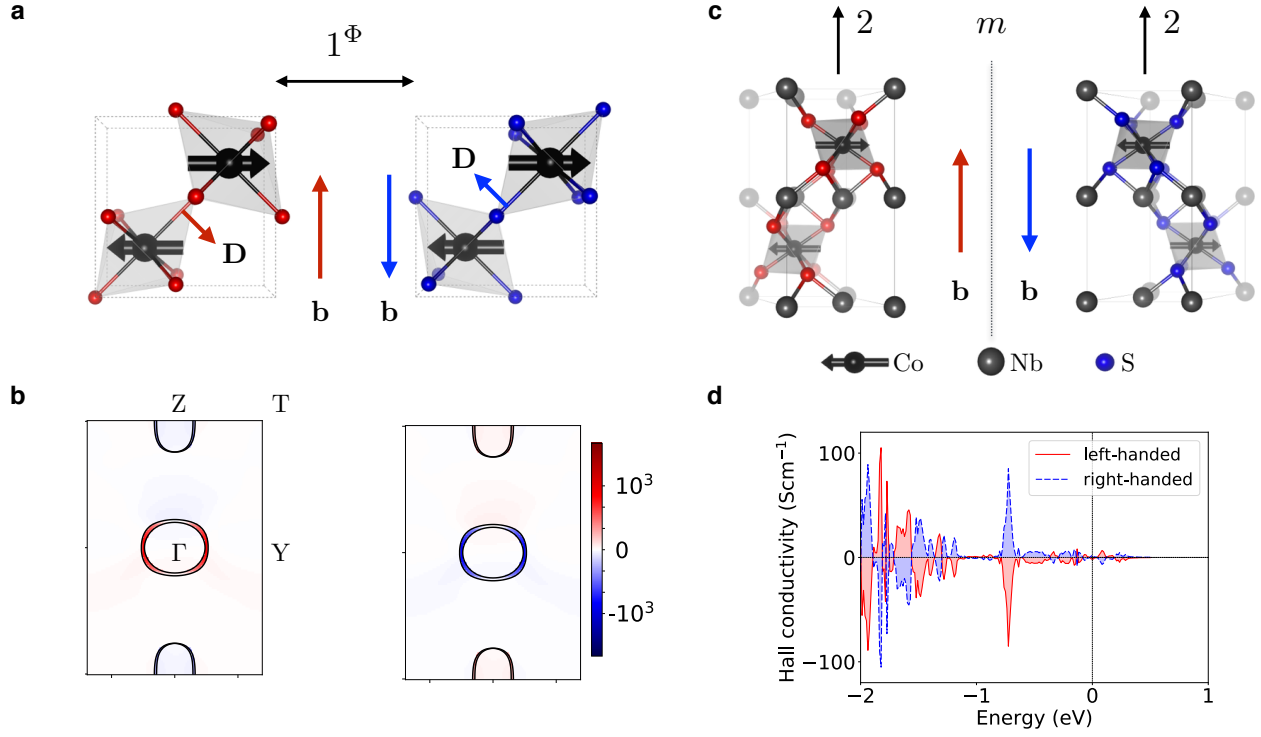


FIG. 4. **Crystal Hall effect control by the local and global crystal chiralities.** **a**, The two crystals with opposite local chiralities (corresponding to opposite local Dzialoshinskii-Moriya vectors  $\mathbf{D}$ ) are related by rotating the oxygen octahedra around the Ru atoms in opposite sense by 90 degrees. The two crystal arrangements connected by a roto-reversal symmetry operation  $1^\Phi$  give opposite sign of the integrated Berry curvature,  $\mathbf{b} \sim \int d\mathbf{k} \Omega(\mathbf{k})$  (red and blue arrows) and the corresponding crystal Hall conductivity. **b**, An explicit illustration of the sign change of the crystal Hall conductivity on the two Berry curvature maps in the  $YZ$  plane corresponding to the two crystals in **a**. **c**, The crystal of  $\text{CoNb}_3\text{S}_6$  antiferromagnet (left, with a left-handed chirality) and its mirror  $m$  image (right, with a right-handed chirality). **d**, The calculated crystal Hall conductivity changes sign when the crystal chirality is reversed from left- to right-handed.